Materials and Design 167 (2019) 107605

Contents lists available at ScienceDirect

Materials and Design

journal homepage: www.elsevier.com/locate/matdes

Microstructural influence on hydrogen permeation and trapping in steels

Michael A. Liu[a], Pedro E.J. Rivera-Díaz-del-Castillo[b], Jesus I. Barraza-Fierro[a], Homero Castaneda[a], Ankit Srivastava[a,*]

[a]Department of Materials Science and Engineering, Texas A&M University, College Station, TX, USA
[b]Department of Engineering, Lancaster University, Lancaster LA1 4YW, UK

HIGHLIGHTS

- Hydrogen ingress and its distribution across various defects and microstructures in three materials are quantified.
- Traps of two potencies, dislocations and grain boundaries (1), and ferrite/cementite interfaces (2) are identified.
- Trap-1 is responsible for trapping hydrogen at early stages of ingress, whereas trap-2 gather hydrogen at later stages.
- Specimen-specimen variation in trapped hydrogen at fixed charging conditions correlate to variations in trap densities.
- Methodology presented allows for microstructure design by simultaneously accounting for hydrogen permeation and binding.

GRAPHICAL ABSTRACT

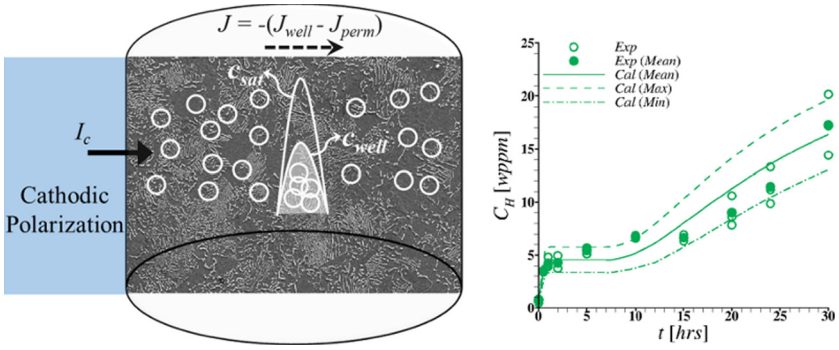

ARTICLE INFO

Article history:
Received 4 November 2018
Received in revised form 8 January 2019
Accepted 13 January 2019
Available online 7 February 2019

Keywords:
Hydrogen diffusion
Hydrogen quantification
Hydrogen embrittlement
Steels
Microstructure
Modeling

ABSTRACT

The microstructural influence on hydrogen permeation and trapping in pure iron and two ferritic-pearlitic steels, AISI 1018 and AISI 4340 is quantified. To this end, hydrogen is introduced into specimens of these materials through electrochemical charging and the total hydrogen content of the specimens are quantified following gas fusion analysis principle. Furthermore, a modeling framework based on Fickian diffusion equations including the relevant microstructural features, electrochemical charging conditions and three-dimensional geometry of the specimen affecting the overall diffusion behavior is adopted to describe the time-dependence of hydrogen content in the three materials. The approach quantitatively describes the hydrogen ingress into the three materials, as well as its distribution across various defects and microstructural features. Traps of two potencies are identified, dislocations and grain boundaries (trap 1), and ferrite/cementite interfaces (trap 2). The former are shown to be responsible for the trapped hydrogen at early stages of its ingress, whereas trap 2 is shown to gather trapped hydrogen at later stages. The ability to design microstructures to control hydrogen ingress and diffusion is discussed, showing how the framework presented here can be adopted for controlling hydrogen in commercial components, and how this can delay hydrogen-related embrittlement.

* Corresponding author.
E-mail address: ankit.sri@tamu.edu (A. Srivastava).

https://doi.org/10.1016/j.matdes.2019.107605

1. Introduction

The presence of hydrogen in structural metals and alloys, especially steels, has proven to be a problem warranting a significant amount of attention for over a century. In steels the presence of hydrogen severely degrades mechanical properties such as ductility, fracture toughness and fatigue life [1-9]. The degrading effect of hydrogen on the mechanical properties of structural metals and alloys is commonly referred to as hydrogen embrittlement [10]. What makes hydrogen particularly deleterious is its extremely small size and high mobility. Even at ambient conditions, hydrogen can diffuse in steels over large distances [11-16]. The extent of hydrogen ingress, as well as its degrading effect on the mechanical properties has been found to strongly depend on the lattice and the microstructure of the material. For example, the extent of hydrogen embrittlement in ferritic steels has been shown to be much greater than that in austenitic stainless steels [17]. The ferritic iron-based alloys and steels exhibit low hydrogen solubility but high diffusivity of hydrogen in the structure [11]. The permeation and diffusion of hydrogen are even more complicated in multiphase microstructures such as ferritic-pearlitic steels. For pearlitic microstructures it has been suggested that hydrogen cannot easily diffuse through the layers of pearlite but can, however, diffuse through the interfaces and grain boundaries [18-21]. Thus, quantifying the microstructural influence on hydrogen ingress is essential to understand and reduce the risk of hydrogen embrittlement in structural metals and alloys.

The mechanisms of hydrogen ingress in a material depend on the ability of hydrogen to enter and diffuse within the bulk as various lattice imperfections and microstructural features either hinder diffusion or act as trapping sites [22-24]. The surface of the specimen represents an initial energy well for hydrogen ingress and diffusion in the bulk [25], while the binding energy of hydrogen with an imperfection or microstructural feature dictates the trapping susceptibility of the hydrogen [22]. The trapping of hydrogen in the bulk of the material has been suggested to reduce the deleterious effect of hydrogen on mechanical properties by reducing the amount of mobile hydrogen in the material [26-29]. Because the trapped hydrogen must overcome a binding energy larger than that for lattice diffusion before it can be released [30]. This clearly suggests that a quantitative understanding of the role of microstructural features on trapping hydrogen can pave the way to designing material microstructures that drastically reduce the risk of hydrogen embrittlement in structural metals and alloys.

A number of experimental methods such as electrochemical permeation testing to determine the rate of adsorption of electrolytic hydrogen and its subsequent diffusivity [31,32], and thermal desorption spectroscopy to estimate the trap binding energy by indirectly measuring the rate of hydrogen release during continuous heating [30,33], have been employed to study hydrogen diffusion in structural metals and alloys with distinct microstructural features. These techniques have provided several insights into hydrogen transport in materials but the interpretation of the results obtained using these techniques is not straightforward especially for complicated microstructures. Also the results are very sensitive to experimental conditions such as charging current and specimen geometry [34-36]. Hence, a comprehensive modeling framework is needed to quantitatively interpret hydrogen-microstructure interactions in complex material microstructures.

Several models have been proposed to understand hydrogen diffusion in the presence of single or multiple trap sites in a material [22,25,37-43]. These models have been applied to understand and interpret results obtained from electrochemical permeation testing and thermal desorption spectroscopy [6,30,44-46]. But there are several factors that limit the applicability of these models, for example, the model proposed by Oriani [22] does not account for kinetic effects and hydrogen interactions with the traps, the Kissinger equation [37] ignores the effect of specimen dimensions and density of traps, whereas the approach for hydrogen transport introduced by McNabb and Foster [38] requires a number of fitting parameters. However, the wide application of Oriani's model [22] to estimate hydrogen diffusivity in various materials suggests that, to an extent, the assumption of local equilibrium between the hydrogen situated in the lattice and in the traps holds and the Fickian diffusion models can describe hydrogen diffusion. Following this, recently, Galindo-Nava et al. [47] introduced a unified modeling framework for hydrogen transport combining electrochemical permeation, thermal desorption and degassing. The modeling framework of Galindo-Nava et al. [47] is based on Fickian diffusion equations including the relevant microstructural features, electrochemical charging conditions and three-dimensional geometry of the specimen that affect the overall diffusion behavior.

The objective of this work is to quantify the microstructural influence on hydrogen permeation and trapping in pure iron and two ferritic-pearlitic steels, AISI 1018 low-carbon steel and AISI 4340 high strength alloy steel. To this end, the initial microstructure of the three materials are thoroughly characterized and the hydrogen is introduced into cylindrical specimens of these materials through electrochemical charging. The total hydrogen content of the specimens are quantified following gas fusion analysis principle commonly termed as melt extraction. The experimentally measured variation of total hydrogen concentration with electrochemical charging time in the specimens of all three materials are then modeled using the modeling framework of Galindo-Nava et al. [47]. The coupled experimental and modeling work allows us to understand and quantify the influence of various defects and microstructural features on hydrogen permeation and trapping. The results presented here reveal that due to the presence of limited hydrogen trap density (grain boundaries and dislocations) in the material microstructure, the hydrogen content in pure iron increases slightly with increasing electrochemical charging time and then tends to saturate. On the other hand in the two ferritic-pearlitic steels, 1018 and 4340 steels, there are at least two types of hydrogen trapping sites with significantly different permeability, diffusivity and saturation concentration of hydrogen. This results in two stage permeation and trapping of hydrogen in both, 1018 and 4340 steels, with increasing electrochemical charging time. In addition, the modeling results also rationalize the specimen to specimen variation in the measured hydrogen concentration values for fixed electrochemical charging times. This quantitative understanding of microstructural influence on hydrogen permeation and trapping in the material not only allows us to better assess the risk of hydrogen embrittlement, but also allows us to identify or design material microstructures that reduce the risk of hydrogen embrittlement.

2. Materials and methods

2.1. Material

The materials considered in this work are commercially pure iron, AISI 1018 low carbon steel and AISI 4340 high strength alloy steel. The rods of diameter 25.4 mm of the commercially pure iron were acquired from the Goodfellow Corporation, and the rods of diameter 12.7 mm of the AISI 1018 and 4340 steels were acquired from the McMaster-Carr Supply Company. The nominal chemical composition of the materials provided by the supplier are as follows: Pure Iron is 99.8% pure with impurities like Mn$<$ 800 ppm, C$<$ 200 ppm, P$<$ 200 ppm and S$<$ 150 ppm; AISI 1018 low carbon steel contains, 98.06–99.42 % Fe, 0.13–0.2 % C, 0.3–0.9 % Mn, 0.04% (max) P, 0.15–0.3 % Si and 0.5% (max) S; and AISI 4340 high strength alloy steel contains, 95.09–96.08 % Fe, 0.38–0.43 % C, 0-0.04% Cr, 0.6–0.8 % Mn, 0.7–0.9 % Mo, 1.65–2 % Ni, 0.35% P, 0.2–0.35 % Si and 0.04% S.

2.2. Metallography

Metallographic studies were performed on all three materials to characterize their initial microstructure using Scanning Electron Microscopy (SEM). The SEM analyses were carried out using a Tescan FERA-3 model GMH Focused Ion Beam Microscope.

2.3. Hydrogen charging experiment

The cylindrical specimens of length and diameter equal to 6.35 mm of all three materials were machined from the as-received rods. Hydrogen was then introduced into cylindrical specimens through electrochemical charging. All the cylindrical specimens were first mechanically polished before initiating the electrochemical charging experiments to facilitate hydrogen ingress. For the electrochemical charging experiments, one end of the cylindrical specimens were spot welded to Nickel wires of diameter 0.73 mm and then inserted into glass tubes. The welded end of the specimens and the bottom of the glass tubes were sealed using adhesive to ensure that in the electrochemical cell only the specimen is exposed to the electrolyte and is the primary conduit for hydrogen adsorption. The electrochemical cell comprised a glass beaker with a rubber cap with two holes: one hole with a diameter of ~6.45 mm to insert the glass tube containing the galvanic wire and the specimen assembly, and a smaller hole to insert the platinum counter electrode. The platinum counter electrode acted as the cathode from the power supply while the specimen acted as the anode. To check the suitability of the platinum counter electrode for use in the electrochemical charging experiments, graphene electrodes were cross-referenced against the charging values of the platinum counter electrode. A comparison of the values generated by both counter electrode materials were within reasonable agreement. The hydrogen charging experiments were carried out at room temperature using 0.5 mol H_2SO_4 solution and 58 mA current for charging times varying from 0.5 to 30 h.

2.4. Quantifying hydrogen content

The hydrogen content in all the cylindrical specimens were determined using G8 Galileo, a high performance O, N and H analyzer by Bruker Corporation. The analyzer works on the inert gas fusion principle also commonly known as melt extraction. The inert gas fusion principle involves fusion of the specimen in a graphite crucible at high temperatures. Post electrochemical charging and pre analysis in the G8 Galileo, all the hydrogen charged cylindrical specimens were mechanically polished to remove the corrosion film, and cleaned using acetone and dry air.

3. Experimental results

The representative microstructures of the commercially pure iron, AISI 1018 low carbon steel and AISI 4340 high strength alloy steel considered in this work are shown in Fig. 1. The microstructure of commercially pure iron is single phase and polycrystalline with average ferritic grains size of ~50 μm, Fig. 1a, while the microstructures of 1018 and 4340 steels are dual phase consisting of ferritic grains and pearlitic (lamellar cementite) particles, Fig. 1b and c. On average the size of ferritic grains in 1018 steel is ~10 μm whereas the size of ferritic grains in 4340 steel is ~6 μm. The average volume fraction of pearlite in 1018 steel is ~22% whereas the average volume fraction of pearlite in 4340 steel is about 60%. As seen in Fig. 1b and c, the microstructure of pearlite in 1018 steel is finer than that in 4340 steel. The average lamellar spacing of pearlite in 1018 steel is ~0.15 μm whereas in 4340 steel the average lamellar spacing is ~0.7 μm.

Hydrogen was introduced into cylindrical specimens of all three materials through electrochemical charging, and the hydrogen content in the specimens, post charging, was quantified using gas fusion principle commonly known as melt extraction as detailed under Section 2. The hydrogen content in several uncharged specimens of all the materials was also quantified. The variation of total hydrogen concentration, C_H, with electrochemical charging time, t, in all three materials, commercially pure iron, AISI 1018 low carbon steel, and AISI 4340 high strength alloy steel are shown in Fig. 2. Each data point in Fig. 2 corresponds to a unique electrochemical charging and hydrogen quantification experiment. To better understand the statistical variations, at least three specimens of each material were analyzed for each electrochemical charging time. As seen in Fig. 2, all the three materials contain initial hydrogen (C_H at $t = 0$) and the initial hydrogen concentration in all three materials varies from specimen to specimen. There is also a specimen to specimen variation in the measured hydrogen concentration value for all electrochemical charging times.

On an average the initial hydrogen concentration (C_H at $t = 0$) in pure iron is ~1.4 wppm, in 1018 steel is ~0.9 wppm, and in 4340 steel is ~ 0.7 wppm. For parameters, such as specimen dimensions, electrolyte and charging current density used here for the hydrogen charging experiments, the average hydrogen concentration in pure iron increases slightly for electrochemical charging times less than an hour and then tends to saturate for higher charging times, Fig. 2a. After three hours of hydrogen charging, the average hydrogen concentration in pure iron is found to be ~2.4 wppm. Although not shown in Fig. 2a, limited hydrogen charging and quantification experiments for pure iron specimens were also carried out for charging times 5 h, 15 h, and 24 h, and on average, the hydrogen concentration was found to be ~2.42 wppm. Similar to pure iron,

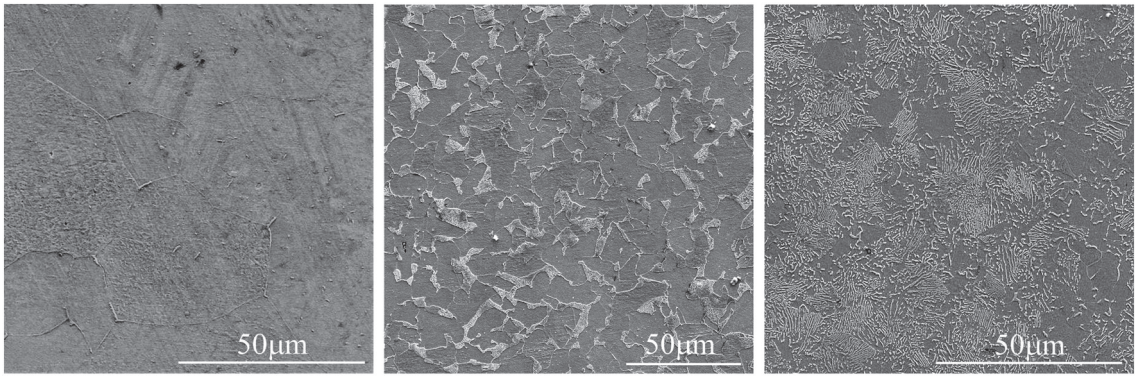

Fig. 1. Representative secondary electron SEM images showing the microstructures of as-received, (a) commercially pure iron, (b) AISI 1018 low carbon steel, and (c) AISI 4340 high strength alloy steel.

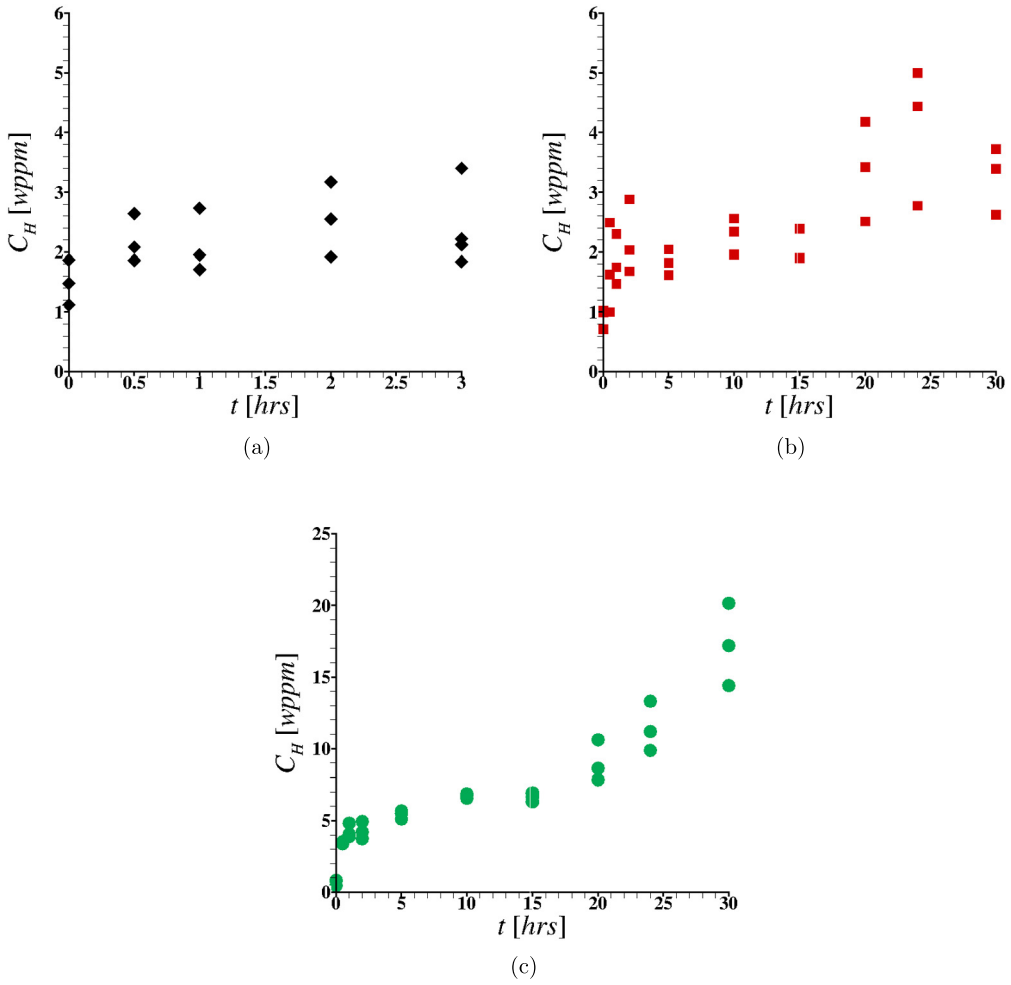

Fig. 2. Experimentally measured variation of hydrogen concentration, C_H, with electrochemical charging time, t, in (a) commercially pure iron, (b) AISI 1018 low carbon steel, and (c) AISI 4340 high strength alloy steel. Each data point corresponds to a unique electrochemical charging and hydrogen quantification experiment, and for each electrochemical charging time at least 3 specimens were analyzed.

in 1018 steel, Fig. 2b, the average hydrogen concentration increases slightly for $t < 1$ h and then tends to saturate for 1–5 h of charging times. After two hours of hydrogen charging, the average hydrogen concentration in 1018 steel is found to be ~2.2 wppm. But unlike pure iron, for charging times greater than ~5 h, the average hydrogen concentration in 1018 steel starts to increase again until 25–30 h of charging times. After 25 h of hydrogen charging, the average hydrogen concentration in 1018 steel is found to be ~4.1 wppm.

The dependence of the measured hydrogen concentration, C_H, in 4340 steel on the electrochemical charging time, t, shown in Fig. 2c is qualitatively similar to that of 1018 steel shown in Fig. 2b. In 4340 steel the average hydrogen concentration increases rapidly for electrochemical charging times within an hour and then tends to saturate for 1–5 h of charging times. After five hours of hydrogen charging, the average hydrogen concentration in 4340 steel is found to be ~5.5 wppm. For charging times greater than ~ 8–10 h, the average hydrogen concentration in 4340 steel starts to increase again. After 30 h of hydrogen charging, the average hydrogen concentration in 4340 steel is found to be ~17.5 wppm. As can be seen in Fig. 2c, the average hydrogen concentration in 4340 steel does not reach a saturation value until $t = 30$ h. Nevertheless, hydrogen charging and quantification experiments were not carried out beyond 30 h because for longer electrochemical charging times the 4340 specimens developed a significant amount of corrosion.

4. Modeling hydrogen permeation during electrochemical charging

4.1. Model formulation

To quantify the microstructural influence on hydrogen permeation and trapping in pure iron and two ferritic-pearlitic steels, 1018 and 4340, during electrochemical charging we rely on the modeling framework developed by Galindo-Nava et al. [47]. For the sake of completeness the key ingredients of the modeling framework by Galindo-Nava et al. [47] are reproduced here. For a complete description of the model the readers are referred to [47] and the references cited therein. The modeling framework of Galindo-Nava et al. [47] is based on Fickian diffusion equations including the relevant microstructural features, electrochemical charging conditions and three-dimensional geometry of the specimen affecting the overall diffusion behavior.

A schematic representation of the diffusion landscape for hydrogen considered in the modeling framework of [47] is shown in Fig. 3. As shown in the figure, after the hydrogen enters the specimen from the cathodic polarization and overcomes the permeation activation energy, the hydrogen atoms diffuse in the lattice until they encounter a trap (concentration well). The trap landscape depends on the microstructure of the material and is described by a function c_{well} with a saturation concentration, c_{sat}. The hydrogen atoms

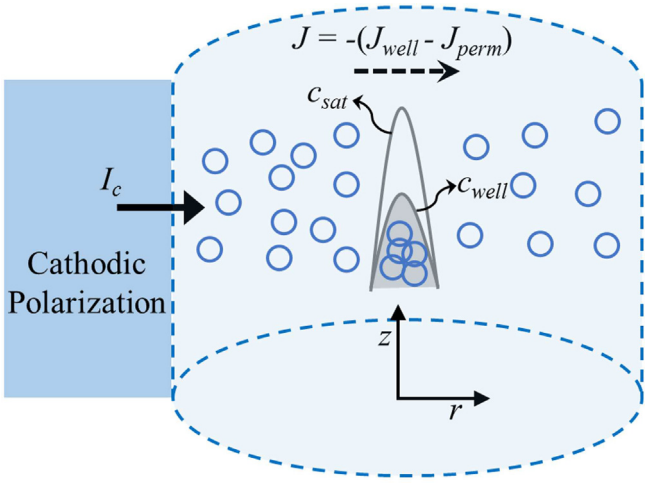

Fig. 3. Schematic representation of flux, J, and concentration, c, landscape for hydrogen transport and entrapment.

are adsorbed to a trap until the well is saturated and the remaining hydrogen atom continue to diffuse through the lattice until the next trap is encountered. The diffusivity of hydrogen in a heterogeneous material microstructure will however vary locally due to the heterogeneous energy landscape. But the modeling framework of Galindo-Nava et al. [47] assumes a homogeneous trapping landscape that is consistent with the assumption of local equilibrium between the free and trapped hydrogen atoms employed by Oriani [22]. The apparent diffusion coefficient during hydrogen permeation is then determined by representing the heterogeneous microstructure as a homogeneous representative volume element as suggested by Frappart et al. [48]. This results in the net mass flux, J, within the specimen being equal to the difference between the flux going to the wells, J_{well}, and the mass flux induced by electrochemical permeation, J_{perm} resulting from the permeated concentration c_{perm} [49]:

$$J = -\left(J_{well} - J_{perm}\right) = -D_{perm}\nabla\left(c_{well} - c_{perm}\right) \tag{1}$$

In Eq. (1), ∇ is the differential operator in three dimensions and D_{perm} is the apparent diffusivity during permeation [35] given as,

$$D_{perm} = D^0_{perm}\sqrt{I_c}\left(1 + \frac{N_t}{N_l}\exp\left(\frac{E_b}{R_g T}\right)\right)\exp\left(-\frac{E_{perm} + Q}{R_g T}\right) \tag{2}$$

where, D^0_{perm} is the apparent diffusion coefficient prefactor, I_c is the cathodic current density, N_l and N_t are the total lattice and trapping sites in the material, respectively, E_b is the trap binding energy with hydrogen, E_{perm} is the permeation activation energy that accounts for the increase in the energy barrier due to hydrogen ingress [48], Q is the activation energy for hydrogen lattice diffusion, R_g is the gas constant and T is the absolute temperature. The apparent diffusion coefficient in Eq. (2), not only includes the effects of microstructure (via N_t, E_b and E_{perm}), but it also accounts for variations in the charging current density, I_c.

The diffusion length of hydrogen can be assumed to be dictated by the mean free path of the traps. Hence, the encountering frequency of hydrogen in the lattice and the trapping wells should be proportional to the mean spacing, Λ, of the respective microstructural features or traps i.e. $N_t/N_l = r_t/\Lambda$, where r_t is the width of the trap. For dislocations, Λ is simply the mean dislocation spacing, $1/\sqrt{\rho}$, where ρ is the dislocation density and $r_t = \pi b$ [43], where b is the Burgers vector. Similarly, for grain boundaries, Λ is the grain size, D_g and for pearlite, Λ is the lamellar spacing, l_p. The width of the trap for both the grain boundaries and the pearlite can be taken to be, $r_t = b$. Following this the number density (N_t/N_l) of traps such as dislocations (N_{dis}/N_l), grain boundaries (N_{gb}/N_l) and pearlite (N_p/N_l) present in the three materials considered in this work can be simply given as,

$$\begin{aligned}\frac{N_{dis}}{N_l} &= \pi b\sqrt{\rho}\\ \frac{N_{gb}}{N_l} &= \frac{b}{D_g}\\ \frac{N_p}{N_l} &= \frac{b}{l_p}\end{aligned} \tag{3}$$

The evolution equation for the hydrogen concentration is then obtained by applying Fick's second law:

$$\frac{\partial c_{perm}}{\partial t} = D_{perm}\nabla^2\left(c_{well} - c_{perm}\right), \tag{4}$$

Eq. (4) for a cylindrical specimen of radius R and length L can be solved by applying the method of separation of variables: $c_{perm} = \theta_{mn}(t)R_n(r)Z_m(z)$. As noted in [47] the variation of c_{well} with r and z is same as c_{perm} since the traps determine the diffusion profile in the specimen [50], i.e. $c_{well} = c_{sat}R_n(r)Z_m(z)$. Eq. (4) is then expressed as,

$$R_nZ_m\dot{\theta}_{mn} = D_{perm}(c_{sat} - \theta_{mn})\left(R_n''Z_m + \frac{1}{r}R_n'Z_m + R_nZ_m''\right) \tag{5}$$

Eq. (5) represents a set of three ordinary differential equations that individually depend on t, r and z. In the absence of initial hydrogen in the specimen, the initial and boundary conditions are,

$$\begin{aligned}&c_{perm}(r,z,t) = 0 \quad at \quad t = 0\\ &c_{perm}(r,z,t) = c_{sat} \quad at \quad r = R\\ &\tfrac{\partial c_{perm}}{\partial r}(r,z,t) = 0 \quad at \quad r = R\\ &c_{perm}(r,z,t) = c_{sat} \quad at \quad z = -L/2, L/2\\ &\tfrac{\partial c_{perm}}{\partial z}(r,z,t) = 0 \quad at \quad z = -L/2, L/2\end{aligned} \tag{6}$$

The solution to Eq. (4) with the initial and boundary conditions in Eq. (6) is given by the series,

$$c_{perm}(r,z,t) = c_{sat}\sum_{m,n=0}^{\infty}\left(1 - \exp\left(-D_{perm}\left(\lambda_n^2 + \alpha_m^2\right)t\right)\right)R_nZ_m \tag{7}$$

where, $\lambda_n = \frac{4n-1}{4R}\pi$ and $\alpha_m = \frac{\pi}{L}m$ are the eigenvalues of Eq. (4), and $R_n = \frac{2}{R\lambda_n J_1(\lambda_n R)}J_0(\lambda_n r)$ and $Z_m = \frac{4}{L\alpha_m}\sin\left(\frac{\pi}{2}m\right)\cos(\alpha_m z)$ are the eigensolutions along r and z, respectively, J_0 is the Bessel function of first kind and zero order in r. Eq. (7) allows us to determine the hydrogen concentration profile for known experimental parameters such as temperature, specimen geometry and charging current density, and material parameters such as defect density, saturation concentration of trapped hydrogen in the trapping wells, permeation energy and binding energy.

4.2. Parametric analysis

The effects of all the experimental and material parameters on the prediction of hydrogen permeation in the specimen using Eq. (7) are coupled and nonlinear. Thus, we carried out parametric studies to understand the effect of few relevant material parameters on the prediction of hydrogen permeation in the specimen. The effect of dislocation density, ρ, saturation hydrogen concentration, c_{sat}, and the effect of permeation, E_{perm}, and binding energies, E_b, on the predicted variation of hydrogen concentration, C_H, with electrochemical charging time, t are shown in Figs. 4 and 5, respectively. In Figs. 4 and 5, $C_H = c_{perm}$. The fixed experimental parameters, specimen

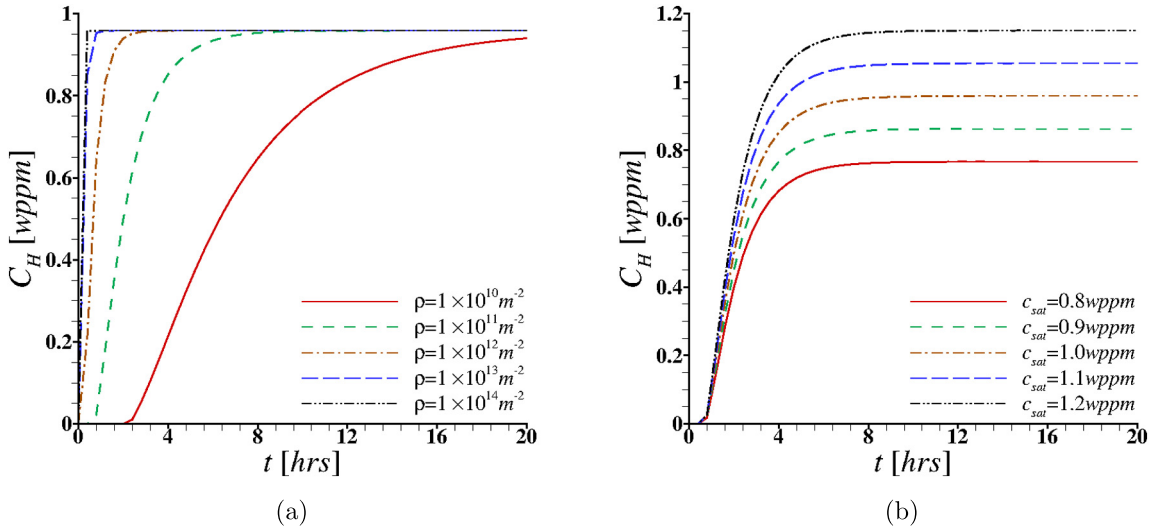

Fig. 4. Results of parametric study to explore the effect of (a) dislocation density, ρ, in Eq. (3) and (b) saturation hydrogen concentration, c_{sat}, in Eq. (7) on the predicted variation of hydrogen concentration, C_H, with electrochemical charging time, t.

geometry and charging current, given in Section 2, are used in the parametric studies. The other constant parameters used in the calculations are, temperature $T = 293$ K and gas constant $R_g = 8.314$ J/mol·K, and the lattice diffusion parameter for ferrite [51]: activation energy $Q = 6.7$ kJ/mol and apparent diffusion coefficient prefactor $D^0_{perm} = 1.16 \times 10^{-11}$ m^3 A$^{-1/2}$ s^{-1}.

For the parametric study to understand the effect of dislocation density, ρ, on the prediction of hydrogen permeation shown in Fig. 4a, the parameters $c_{sat} = 1$ wppm, $E_{perm} = 10$ kJ/mol, and $E_b = 35$ kJ/mol, are assumed. The parameter ρ enters as defect density, N_t/N_l (Eq. (3)), in Eq. (7) through Eq. (2). To estimate the defect density corresponding to ρ using Eq. (3), the Burgers vector $b = 0.285$ nm for ferrite is assumed. As shown in Fig. 4a, for all other parameters being fixed, the amount of dislocation density affects both the onset of hydrogen permeation (t at $C_H > 0$) and attainment of saturation of hydrogen content in the specimen (t at $C_H \to c_{sat}$), such that increasing ρ decreases both t at $C_H > 0$ and t at $C_H \to c_{sat}$. Similarly, for the parametric study to understand the effect of saturation hydrogen concentration, c_{sat}, on the prediction of hydrogen permeation shown in Fig. 4b, the parameters $\rho = 1 \times 10^{11}$ m^{-2}, $E_{perm} = 10$ kJ/mol, and $E_b = 35$ kJ/mol, are assumed. The parameter c_{sat} directly enters the Eq. (7). As shown in Fig. 4b, for all other parameters being fixed, the saturation hydrogen concentration in the trapping well only affects the maximum hydrogen content in the specimen.

Next, the results of the parametric study to understand the effect of permeation energy, E_{perm}, on the prediction of hydrogen permeation is shown in Fig. 5a. For this study the parameters $c_{sat} = 1$ wppm, $\rho = 1 \times 10^{11}$ m^{-2}, and $E_b = 35$ kJ/mol, are assumed. The parameter E_{perm} enters Eq. (7) through Eq. (2). As shown in Fig. 5a, for all other parameters being fixed, increasing E_{perm} increases both t at $C_H > 0$ and t at $C_H \to c_{sat}$. Similarly, the results of parametric study to understand the effect of binding energy, E_b, on the prediction of hydrogen permeation is shown in Fig. 5b. For this study the parameters $c_{sat} = 1$ wppm, $\rho = 1\times 10^{11}$m^{-2}, and $E_{perm} = 10$ kJ/mol, are assumed. The parameter E_b enters Eq. (7) through Eq. (2). As shown in Fig. 5b, for all other parameters being fixed, increasing E_b decreases both t at $C_H > 0$ and t at $C_H \to c_{sat}$.

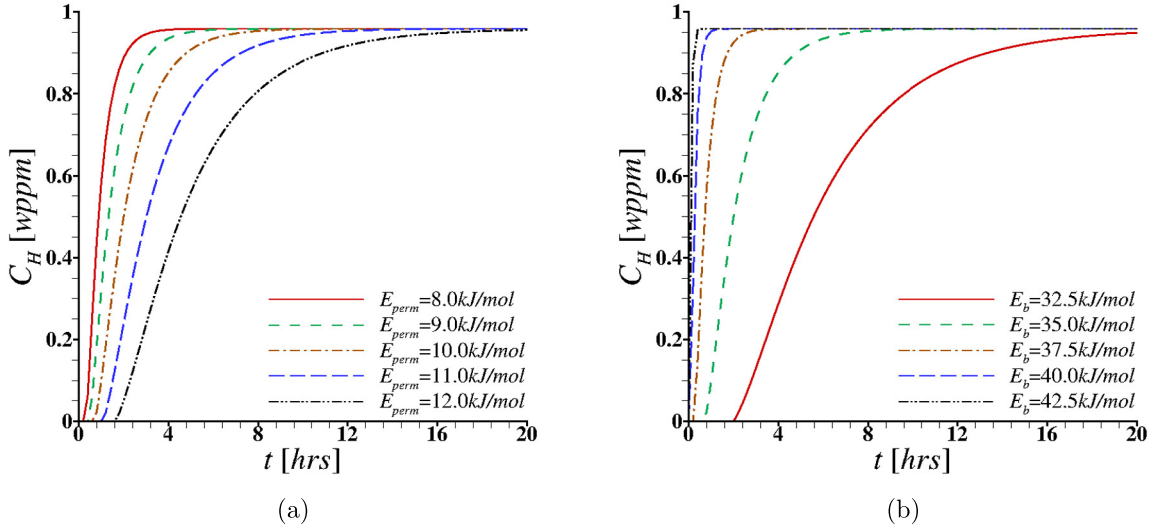

Fig. 5. Results of parametric study to explore the effect of (a) permeation energy, E_{perm}, in Eq. (2) and (b) binding energy, E_b, in Eq. (2) on the predicted variation of hydrogen concentration, C_H, with electrochemical charging time, t.

5. Modeling results and discussion

We now use the modeling framework detailed in Section 4 to calculate the variation of total hydrogen concentration, C_H, with electrochemical charging time, t, in pure iron and the two ferritic-pearlitic steels, 1018 and 4340, and compare the predictions with the experimental results presented in Section 3. Our goal is to understand and quantify the microstructural influence on hydrogen permeation and trapping. In all the calculations the specimen geometry and charging current are kept fixed as in the experiments, see Section 2 for the details of the experimental procedure. The other parameters that enter the modeling framework, and are considered constant in all the calculations are, temperature $T = 293$ K and gas constant $R_g = 8.314$ J/mol·K, and we consider ferrite as the matrix phase for the three materials, so that the lattice diffusion parameter for ferrite [51]: activation energy $Q = 6.7$ kJ/mol and apparent diffusion coefficient prefactor $D^0_{perm} = 1.16 \times 10^{-11}$ m^3 A$^{-1/2}$ s^{-1}, are also considered constant in all the calculations. But the parameters such as defect density (N_t/N_l), saturation concentration of trapped hydrogen in the trapping wells (c_{sat}), permeation energy (E_{perm}) and binding energy (E_b) are assumed to depend on specific material and relevant microstructural features. In addition, we assume that the total hydrogen concentration (C_H) measured using the procedure outlined in Section 2 predominantly represents the trapped hydrogen concentration because of low solubility of hydrogen in ferrite.

5.1. Commercially pure Fe

The microstructure of commercially pure iron is single phase and polycrystalline, Fig. 1a. Thus in extruded rods of pure iron the hydrogen traps are simply the grain boundaries and the dislocations. Based on the quantitative characterization of the microstructure of pure iron, we take the ferrite grain size, D_g, in the material to be 50±10 μm. The dislocation density in the material is not measured in this work but following Galindo-Nava et al. [47], the dislocation density is assumed to be, $\rho = 5 \pm 2.5 \times 10^{14}$ m^{-2}. This range of values of D_g and ρ are then used to estimate the range of total defect density as $N_t/N_l = \pi b\sqrt{\rho} + b/D_g$ (see Eq. (3)), where $b = 0.285$ nm for ferrite is assumed. Next, we focus on estimating the saturation concentration of trapped hydrogen, c_{sat}, at grain boundaries and dislocations in pure iron. The saturation concentration of hydrogen has been found to increase with increase in the charging current density, I_c, [36, 45, 52-54] according to $c_{sat} \propto I_c^{1/2}$. Additionally, c_{sat} has been found to depend on the density of the trapping sites, N_t/N_l [34]. Combining these gives $c_{sat} \propto I_c^{1/2} N_t/N_l$. Since in this work I_c is fixed, we assume that any variation in the saturation hydrogen concentration is predominantly due to specimen to specimen variation in the defect density giving, $c_{sat} = \left(c_{sat}^{avg}/(N_t/N_l)^{avg}\right) N_t/N_l$. Here, c_{sat}^{avg} is the average saturation concentration of trapped hydrogen and is estimated from the experimental measurements by subtracting the average value of C_H at $t = 0$ from the average value of C_H at $t = 3$ h, while $(N_t/N_l)^{avg}$ is simply the average defect density. The other two material parameters that enter the modeling framework are E_{perm} and E_b. The value of E_{perm} is taken to be 13 kJ/mol following the range of values reported in literature [31,32,55], while the value of E_b is found to be 36 kJ/mol in order to better represent the experimental measurements. The value of the binding energy, $E_b = 36$ kJ/mol, is within the general range of the values of binding energies reported for grain boundaries and dislocations in pure iron [30,43,56-58].

Now with all the parameters defined, we calculate the variation of c_{perm} with electrochemical charging time, t, in pure iron using Eq. (7) for the range of defect density, N_t/N_l. The calculated variation of hydrogen concentration, $C_H = c_{perm}$, with electrochemical charging time, t, in the traps, grain boundaries and dislocations, is shown in Fig. 6a. The mean value of $C_H(t)$ in the traps is shown by a solid line while the dashed line is the mean value plus one standard deviation (max) and the dashed-dot line is the mean minus one standard deviation (min) of the value of $C_H(t)$. The variation in C_H for a fixed t is due to the variations in D_g and ρ, that results in variation in the value of N_t/N_l that affects both D_{perm} and c_{sat}. Finally, the total hydrogen concentration in the specimens of pure iron are estimated as, $C_H(t) = C_H^0 + c_{perm}(t)$, so that the value of $C_H(t)$ accounts for both the variations in $c_{perm}(t)$ and the variations in the initial hydrogen concentration C_H at $t = 0$ (C_H^0) observed in the experimental measurements. The calculated variation of total hydrogen concentration, C_H, with electrochemical charging time, t, in commercially pure iron is compared with the experimental measurements in Fig. 6b. From Fig. 6b, a very good correlation between the calculated and the experimental average values of $C_H(t)$ is noted. Additionally, most experimental data lie within the plus/minus one standard deviation of the calculated values of $C_H(t)$.

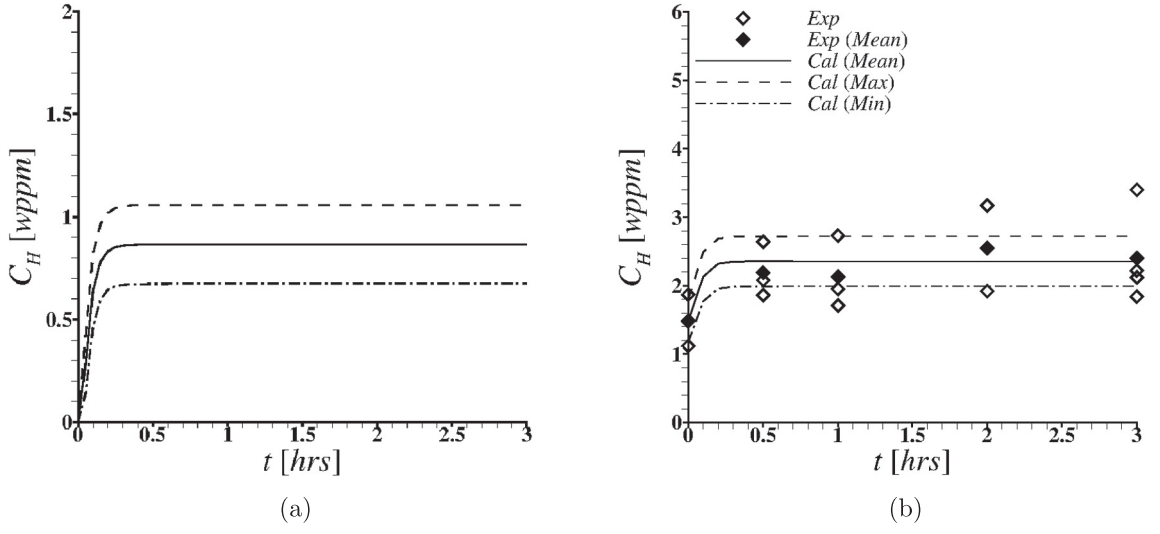

Fig. 6. Commercially pure Fe. (a) Calculated variation of hydrogen concentration, C_H, with electrochemical charging time, t, in the traps (Grain Boundaries and Dislocations) present in pure iron. In (a) the solid line is the mean value of $C_H(t)$, the dashed line is the mean value plus one standard deviation (max) and the dashed-dot line is the mean minus one standard deviation (min) of the value of $C_H(t)$. (b) Comparison of calculated (cal) and experimentally (exp) measured variation of total hydrogen concentration, C_H, with electrochemical charging time, t.

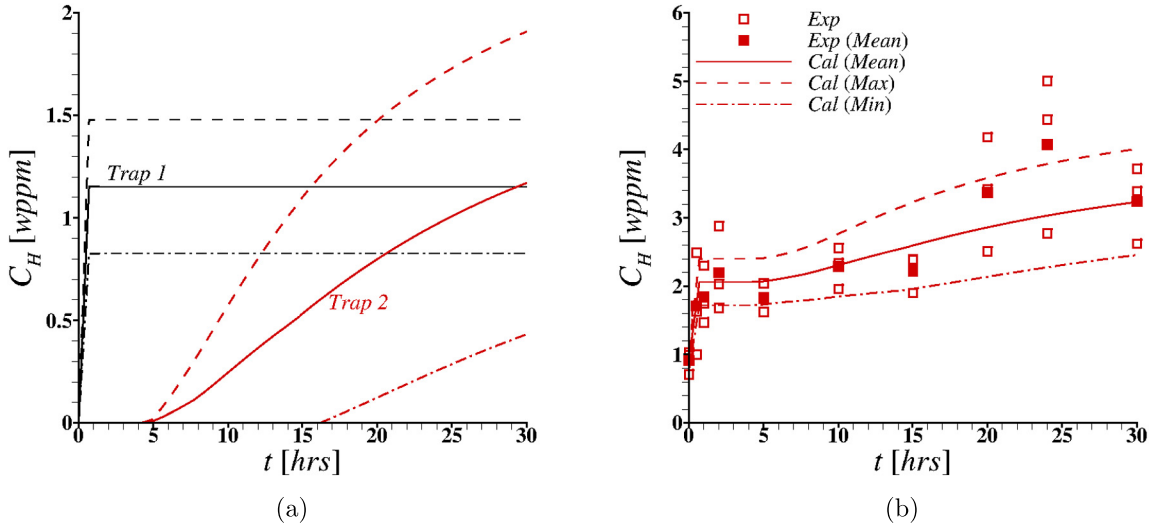

Fig. 7. AISI 1018 low carbon steel. (a) Calculated variation of hydrogen concentration, C_H, with electrochemical charging time, t, in the two traps (1. Grain Boundaries and Dislocations, and 2. Ferrite/Cementite Interface) present in 1018 steel. In (a) the solid lines are the mean value of $C_H(t)$, the dashed lines are the mean value plus one standard deviation and the dashed-dot lines are the mean minus one standard deviation of the value of $C_H(t)$. (b) Comparison of calculated (cal) and experimentally (exp) measured variation of total hydrogen concentration, C_H, with electrochemical charging time, t.

5.2. AISI 1018

As shown in Fig. 2b, similar to pure iron, the average hydrogen concentration in 1018 steel increases slightly for electrochemical charging times $t < 1$ h and then tends to saturate for $1 - 5$ h of charging times. But unlike pure iron for charging times greater than ~5 h, the average hydrogen concentration in 1018 steel starts to increase again. The two stage permeation and trapping of hydrogen in 1018 steels suggests that there are two types of hydrogen traps in this material. We start with the assumption that the two types of hydrogen traps in 1018 steel are ferrite grain boundaries and dislocations in ferrite, and ferrite/cementite interfaces in the pearlitic microstructure. The ferrite grain size, D_g, in the 1018 steel is 10±2 μm whereas the dislocation density, ρ, in the material is assumed to be 5±2.5 × 10^{14} m^{-2}. This range of values of D_g and ρ are then used to estimate the range of total density of trap 1 as $(N_t/N_l)_{Trap\ 1} = (1-f_p)\,(\pi b\sqrt{\rho} + b/D_g)$, where $f_p = 22 \pm 5\%$ is the range of volume fraction of pearlite in 1018 steel. Similarly, the lamellar spacing of pearlite, l_p, in 1018 steel is 0.15 ± 0.05μm, that gives a total density of trap 2 as $(N_t/N_l)_{Trap\ 2} = (f_p)\,(b/l_p)$. The average saturation concentration of hydrogen in trap 1, $\left(c_{sat}^{avg}\right)_{Trap\ 1}$, is taken to be 1.2 wppm, and the value of $\left(c_{sat}^{avg}\right)_{Trap\ 2} = 1.8$ wppm, is considered based on the experimental measurements. The variations in the density of the two traps are then used to estimate the variation in the respective saturation concentration of hydrogen in the traps following, $c_{sat} = \left(c_{sat}^{avg}/(N_t/N_l)^{avg}\right)(N_t/N_l)$. For trap 1, the values of $(E_{perm})_{Trap\ 1} = 13$ kJ/mol and $(E_b)_{Trap\ 1} = 36$ kJ/mol are considered, as was for pure iron. For trap 2, the values of $(E_{perm})_{Trap\ 2} = 10$ kJ/mol and $(E_b)_{Trap\ 2} = 28$ kJ/mol are found to better represent the experimental measurements. The significantly lower binding energy for trap 2, ferrite/cementite interfaces in the pearlitic microstructure, compared to trap 1, ferrite grain boundaries and dislocations in ferrite, results in significantly lower diffusivity of hydrogen through trap 2 compared to trap 1, in line with other observations [59,60].

We separately calculate the evolution of hydrogen concentration, C_H, with electrochemical charging time, t, in the two traps. For trap 1, $C_H = (c_{perm})_{Trap\ 1}$ and for trap 2, $C_H = (c_{perm})_{Trap\ 2}$. The calculated variation of $C_H = (c_{perm})_{Trap\ 1}$ and $C_H = (c_{perm})_{Trap\ 2}$ with t, in the two traps are shown in Fig. 7a. The mean value of $C_H(t)$ in the traps are shown by the solid lines while the dashed lines are the mean value plus one standard deviation (max) and the dashed-dot lines are the mean minus one standard deviation (min) of the values of $C_H(t)$. The variation in C_H at a fixed t for trap 1 is due to the variations in f_p, D_g and ρ, while for trap 2 is due to variations in f_p and l_p. As seen in Fig. 7a, the hydrogen concentration increases rapidly in trap 1 and reaches saturation way before hydrogen starts to permeate into trap 2. The total hydrogen in the specimens of 1018 steel consisting of the two traps are now estimated as, $C_H(t) = C_H^0 + c_{perm}(t)_{Trap\ 1} + c_{perm}(t)_{Trap\ 2}$, so that the value of $C_H(t)$ in the specimen accounts for the variations in $c_{perm}(t)$ in both the traps and the variations in the initial hydrogen concentration C_H at $t = 0$ (C_H^0) observed in the experimental measurements. The calculated variation of total hydrogen concentration, C_H, with t in 1018 steel specimens is compared with the experimental measurements in Fig. 7b. From Fig. 7b, a very good correlation between the calculated and the experimental average values of $C_H(t)$ is noted. Also, most experimental data lie within the plus/minus one standard deviation of the calculated values of $C_H(t)$, although few exceptions exist.

5.3. AISI 4340

The permeation and trapping of hydrogen in 4340 steel are qualitatively similar to that of 1018 steel as shown in Fig. 2b and c, and the microstructures of both the steels are dual phase consisting of ferritic grains and pearlitic (lamellar cementite) particles, Fig. 1b and c. Thus, here as well we start with the assumption that there are two types of hydrogen traps in 4340 steel: ferrite grain boundaries and dislocations in ferrite, and ferrite/cementite interfaces in the pearlitic microstructure. The ferrite grain size, D_g, in the 4340 steel is 6 ± 2μm whereas the dislocation density, ρ, in the material is assumed to be 5 ± 2.5 × 10^{14} m^{-2}. This range of values of D_g and ρ are then used to estimate the range of total density of trap 1 as $(N_t/N_l)_{Trap\ 1} = (1-f_p)\,(\pi b\sqrt{\rho} + b/D_g)$, where $f_p = 60 \pm 5\%$ is the range of volume fraction of pearlite in the steel. Similarly, the lamellar spacing of pearlite, l_p, in 4340 steel is 0.7 ± 0.1μm, that gives a total density of trap 2 as $(N_t/N_l)_{Trap\ 2} = (f_p)\,(b/l_p)$. The average saturation concentration of hydrogen in trap 1, $\left(c_{sat}^{avg}\right)_{Trap\ 1}$, is taken to be 4 wppm, and the value of $\left(c_{sat}^{avg}\right)_{Trap\ 2} = 20$ wppm, is considered based on the experimental measurements. The variations in the

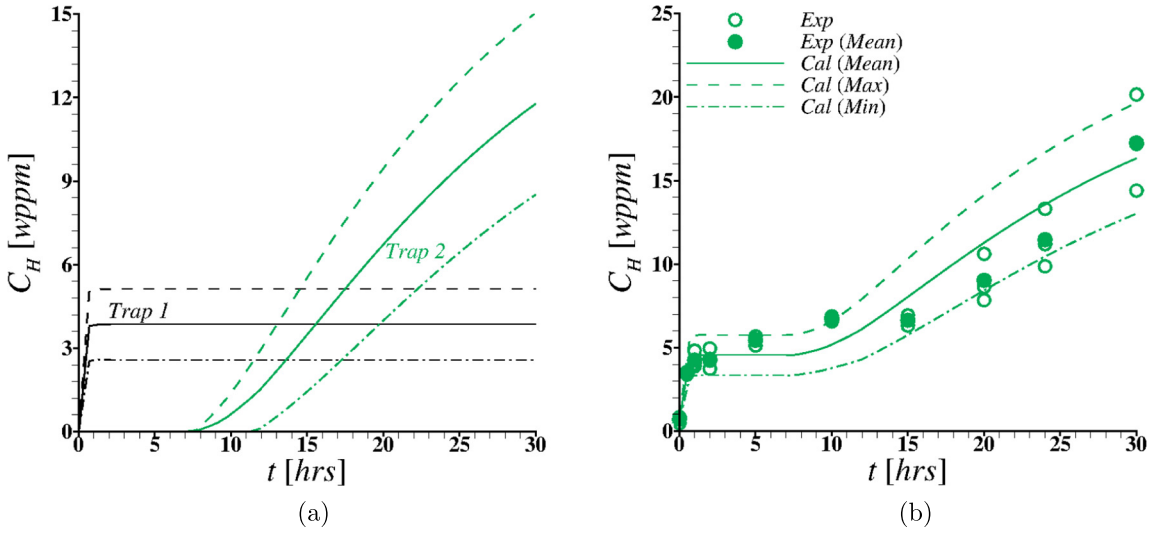

Fig. 8. AISI 4340 high strength alloy steel. (a) Calculated variation of hydrogen concentration, C_H, with electrochemical charging time, t, in the two traps (1. Grain Boundaries and Dislocations, and 2. Ferrite/Cementite Interface) present in 4340 steel. In (a) the solid lines are the mean value of $C_H(t)$, the dashed lines are the mean value plus one standard deviation and the dashed-dot lines are the mean minus one standard deviation of the value of $C_H(t)$. (b) Comparison of calculated (cal) and experimentally (exp) measured variation of total hydrogen concentration, C_H, with electrochemical charging time, t.

density of the two traps are then used to estimate the variation in the respective saturation concentration of hydrogen in the traps following, $c_{sat} = \left(c_{sat}^{avg}/(N_t/N_l)^{avg}\right)(N_t/N_l)$. For trap 1, the values of $(E_{perm})_{Trap\ 1} = 13$ kJ/mol and $(E_b)_{Trap\ 1} = 36$ kJ/mol are considered, as was for pure iron. For trap 2, the value of $(E_b)_{Trap\ 2} = 28$ kJ/mol is considered, as was for 1018 steel but the value of $(E_{perm})_{Trap\ 2} = 9$ kJ/mol is found to better represent the experimental measurements of 4340 steel specimens. The slightly lower permeation energy for trap 2 in 4340 steel compared to 1018 steel can be due to coarser pearlitic microstructure in 4340 steel compared to 1018 steel.

The calculated variation of $C_H = (c_{perm})_{Trap\ 1}$ and $C_H = (c_{perm})_{Trap\ 2}$ with electrochemical charging time, t, in the two traps are shown in Fig. 8a. The mean value of $C_H(t)$ in the traps are shown by the solid lines while the dashed lines are the mean value plus one standard deviation (max) and the dashed-dot lines are the mean minus one standard deviation (min) of the values of $C_H(t)$. The variation in the value of C_H for a fixed t for trap 1 is due to the variations in f_p, D_g and ρ, while for trap 2 is due to variations in f_p and l_p. Similar to 1018 steel, for 4340 steel as well, the hydrogen concentration increases rapidly in trap 1 and reaches saturation way before hydrogen starts to permeate into trap 2. Finally, the total hydrogen in the specimens of 4340 steel consisting of the two traps are estimated as, $C_H(t) = C_H^0 + c_{perm}(t)_{Trap\ 1} + c_{perm}(t)_{Trap\ 2}$. The calculated variation of total hydrogen concentration, C_H, with t in 4340 steel specimens is compared with the experimental measurements in Fig. 8b. From Fig. 8b, a very good correlation between the calculated and the experimental average values of $C_H(t)$ is noted. Also, most experimental data lie within the plus/minus one standard deviation of the calculated values of $C_H(t)$.

5.4. Relating microstructure to permeation and trapping

The modeling results presented here clearly highlight the microstructural influence on hydrogen permeation and trapping in the specimens of pure iron and two ferritic-pearlitic steels, AISI 1018 low-carbon steel and AISI 4340 high strength alloy steel 1018 steels. In particular, the results quantitatively show that, (i) unlike pure iron, there are at least two types of hydrogen trapping sites in 1018 and 4340 steels with significantly different permeation activation and binding energies, (ii) the apparent diffusivity of hydrogen in trap 1 (ferrite grain boundaries and dislocations in ferrite) is greater than that in trap 2 (ferrite/cementite interfaces in the pearlitic microstructure), (iii) the difference in the apparent diffusivity of the two traps results in two stage permeation and trapping of hydrogen in both 1018 and 4340 steels with increasing electrochemical charging times, and (iv) the saturation concentration of hydrogen in trap 1 is less than that in trap 2 in both 1018 and 4340 steels. The estimated permeation activation and binding energies for the three materials and microstructural features therein show that the permeation of hydrogen is easy through the ferrite/cementite interfaces in the pearlitic microstructure compared to grain boundaries and dislocations. But the grain boundaries and dislocations act as stronger hydrogen traps than the ferrite/cementite interfaces in the pearlitic microstructure. Also the ease of permeation of hydrogen through coarse pearlitic microstructure is slightly greater than fine pearlitic microstructure. Lastly, the modeling results also rationalize the specimen to specimen variation in the measured hydrogen concentration values for fixed electrochemical charging times. Here we have shown that most experimental measurements for all three materials lie within plus/minus one standard deviation of the calculated values that is due to variations in the defect/trap densities leading to variations in both the apparent diffusivity and saturation concentration of hydrogen in the traps.

5.5. Microstructure design against hydrogen embrittlement

There are two key aspects in the control and prevention of hydrogen embrittlement: ingress and diffusion. Hydrogen embrittlement necessitates reaching a critical hydrogen concentration for crack propagation. The results presented here demonstrate that material and component design against hydrogen embrittlement requires the consideration of the synergistic contribution of permeation as a result of exposure to a certain environment, as well as diffusion within the material or the component. Designing material microstructures by tailoring hydrogen trapping sites is not sufficient as microstructure is intrinsically related to permeation via E_{perm}. The ferrite/cementite interface displays a value of $(E_{perm})_{Trap\ 2} = 10$ kJ/mol for AISI 1018 whereas $(E_{perm})_{Trap\ 2} = 9$ kJ/mol better describes the experimental results for AISI 4340. Such a 10% decrease in the barrier for permeation can be ascribed to the difference in

the pearlitic structure between both grades; where AISI 1018 and 4340 respectively display an interlamellar spacing of 0.15 and 0.7 μm and a volume fraction of 22 and 60%. Nevertheless, both grades display the same value of $(E_b)_{Trap\ 2} = 28$ kJ/mol. This demonstrates that microstructure simultaneously influences hydrogen ingress and trapping, and alloy and component design has to consider both aspects, and not just trapping as in the previous work by one of the authors [60].

The two-step hydrogen concentration increase in the bulk, C_H is significantly altered by the trapping potency of the different microstructural features. Grain boundaries and dislocations (trap 1), with $(E_{perm})_{Trap\ 1} = 13$ kJ/mol and $(E_b)_{Trap\ 1} = 36$ kJ/mol, differ from ferrite/cementite interfaces (trap 2) with $(E_{perm})_{Trap\ 2} = 9.5 \pm 0.5$ kJ/mol and $(E_b)_{Trap\ 2} = 28$ kJ/mol. Both the trap binding energy and the permeation activation energy are higher for grain boundaries and dislocations compared to the ferrite/cementite interfaces. The effect of these on hydrogen diffusion is dictated by Eq. (2), which shows that trap 1 will bind more strongly with H, increasing D_{perm}; this is consistent with Fig. 5b, where a larger value of E_b significantly accelerates H uptake; conversely, the higher value of E_{perm} will decrease the H uptake, but its effect is more moderate as highlighted by Fig. 5a. It is therefore concluded that the balance between the permeation activation energy and the binding energy of the various traps dictate the inflexion points in multiphase steels; these are manifested by the plateaus in Figs. 7b and 8a. We therefore propose that, in multiphase steels, binding and permeation energies of the constituent phases are accounted for simultaneously to control the content of hydrogen under a critical value dictated by the application. The methodology provided in this work allows for the design of microstructures by simultaneously accounting for both permeation and binding, this would allow to keep the hydrogen content under a critical value beyond which failure may occur.

6. Conclusions

In this work we have quantified the microstructural influence on hydrogen permeation and trapping in pure iron and two ferritic-pearlitic steels, AISI 1018 low-carbon steel and AISI 4340 high strength alloy steel. The initial microstructure of the three materials were thoroughly characterized and the hydrogen was introduced into cylindrical specimens of these materials through electrochemical charging. The total hydrogen content of the specimens were then quantified following gas fusion analysis principle commonly termed as melt extraction. Furthermore, the experimentally measured variation of hydrogen concentration with electrochemical charging time in the specimens of all three materials were modeled using a modeling framework based on Fickian diffusion equations including the relevant microstructural features, electrochemical charging conditions and three-dimensional geometry of the specimen that affect the overall diffusion behavior. The approach presented here to quantify the microstructural influence on hydrogen permeation and trapping in the material will not only allow us to better assess the risk of hydrogen embrittlement, but will potentially also allow us to identify or design material microstructures that reduce the risk of hydrogen embrittlement.

The most significant conclusions of this work are:

1. The hydrogen content in pure iron increases slightly with increasing electrochemical charging time and then tends to saturate. On the other hand, the two ferritic-pearlitic steels, 1018 and 4340 steels, exhibit two stage permeation and trapping of hydrogen with increasing electrochemical charging time.
2. The two stage permeation and trapping of hydrogen in 1018 and 4340 steels are shown to be due to the presence of two types of hydrogen trapping sites (trap 1: ferrite grain boundaries and dislocations, and trap 2: ferrite/cementite interfaces in the pearlitic microstructure) with significantly different permeation activation and binding energies.
3. The apparent diffusivity of hydrogen in trap 1 is found to be greater than that in trap 2, whereas the saturation concentration of hydrogen for trap 1 is found to be less than that for trap 2 in ferritic-pearlitic microstructures.
4. The experimentally measured specimen to specimen variation in hydrogen concentration values for fixed electrochemical charging times for all three materials predominantly lies within plus/minus one standard deviation of the calculated values. In the calculations the variations in hydrogen concentration values for fixed electrochemical charging times is due to variations in the defect/trap densities leading to variations in both the apparent diffusivity and saturation concentration of hydrogen in the traps.
5. The methodology presented in this paper demonstrates that hydrogen permeation and binding energies must be simultaneously considered to quantify hydrogen ingress. In the case of multiphase steels, those quantities can be tailored to ensure the content of hydrogen is kept under a certain limit beyond which failure may occur.

Author contributions

AS, HC and PEJRDC conceptualized the research and secured the funding. MAL carried out the metallography experiments. MAL together with JIBF carried out the hydrogen charging and quantification experiments. AS, PEJRDC and MAL carried out the modeling work. AS, PEJRDC and HC wrote the manuscript with input from all other authors.

Funding

Financial support provided by the American Chemical Society - Petroleum Research Fund # 57643 - DNI10 to AS is gratefully acknowledged. PEJRDC is grateful to the UK Engineering and Physical Sciences Research Council (EPSRC) for support via grant EP/L014742/1.

Declaration of interest

We declare we have no competing interests.

Data availability

This article has no additional data. All experimental and analytical results are reproducible.

Acknowledgments

We thank Professor Michael J. Demkowicz, Department of Materials Science and Engineering, Texas A&M University, College Station, TX, for providing us access to the G8 Galileo ON/H instrument by Bruker Corporation. The open access publishing fees for this article have been covered by the Texas A&M University Open Access to Knowledge Fund (OAKFund), supported by the University Libraries and the Office of the Vice President for Research.

References

[1] W.H. Johnson, On some remarkable changes produced in iron and steel by the action of hydrogen and acids, Nature 11 (1875) 393.
[2] J. Ciruna, H. Szieleit, The effect of hydrogen on the rolling contact fatigue life of AISI 52100 and 440C steel balls, Wear 24 (1) (1973) 107–118.

[3] I.-O. Shim, J. Byrne, A study of hydrogen embrittlement in 4340 steel I: mechanical aspects, Mater. Sci. Eng. A 123 (2) (1990) 169–180.
[4] Y. Kim, Y. Chao, M.J. Pechersky, M.J. Morgan, On the effect of hydrogen on the fracture toughness of steel, Int. J. Fract. 134 (3-4) (2005) 339–347.
[5] S. Wang, M.L. Martin, P. Sofronis, S. Ohnuki, N. Hashimoto, I.M. Robertson, Hydrogen-induced intergranular failure of iron, Acta Mater. 69 (2014) 275–282.
[6] T. Doshida, K. Takai, Dependence of hydrogen-induced lattice defects and hydrogen embrittlement of cold-drawn pearlitic steels on hydrogen trap state, temperature, strain rate and hydrogen content, Acta Mater. 79 (2014) 93–107.
[7] J. Venezuela, Q. Liu, M. Zhang, Q. Zhou, A. Atrens, The influence of hydrogen on the mechanical and fracture properties of some martensitic advanced high strength steels studied using the linearly increasing stress test, Corros. Sci. 99 (2015) 98–117.
[8] X. Li, J. Zhang, Y. Wang, S. Shen, X. Song, Effect of hydrogen on tensile properties and fracture behavior of PH 13-8 Mo steel, Mater. Des. 108 (2016) 608–617.
[9] M. Masoumi, L.P. Santos, I.N. Bastos, S.S. Tavares, M.J. da Silva, H.F. de Abreu, Texture and grain boundary study in high strength Fe-18Ni-Co steel related to hydrogen embrittlement, Mater. Des. 91 (2016) 90–97.
[10] H. Rogers, Hydrogen embrittlement of metals: atomic hydrogen from a variety of sources reduces the ductility of many metals, Science 159 (3819) (1968) 1057–1064.
[11] M. Aucouturier, Grain boundary segregations and hydrogen embrittlement, J. Phys. Colloq. 43 (C6) (1982) C6–175.
[12] H.J. Grabke, E. Riecke, Absorption and diffusion of hydrogen in steels, Mater. Tehnol. 34 (6) (2000) 331.
[13] I. Robertson, H. Birnbaum, P. Sofronis, Hydrogen effects on plasticity, Dislocations in Solids, 15, 2009, pp. 249–293.
[14] P. Lang, M. Rath, E. Kozeschnik, P.E. Rivera-Diaz-del Castillo, Modelling the influence of austenitisation temperature on hydrogen trapping in Nb containing martensitic steels, Scr. Mater. 101 (2015) 60–63.
[15] T. Depover, E. Wallaert, K. Verbeken, On the synergy of diffusible hydrogen content and hydrogen diffusivity in the mechanical degradation of laboratory cast Fe-C alloys, Mater. Sci. Eng. A 664 (2016) 195–205.
[16] R. Miresmaeili, A. Abdollah-Zadeh, The mutual effects of hydrogen and microstructure on hardness and impact energy of SMA welds in X65 steel, Mater. Sci. Eng. A 679 (2017) 87–94.
[17] M. Louthan, Jr, G. Caskey, Jr, Hydrogen transport and embrittlement in structural metals, Int. J. Hydrog. Energy 1 (3) (1976) 291–305.
[18] S. Chan, J. Charles, Effect of carbon content on hydrogen occlusivity and embrittlement of ferrite-pearlite steels, Mater. Sci. Technol. 2 (9) (1986) 956–962.
[19] H.-L. Lee, S.L.-I. Chan, Hydrogen embrittlement of AISI 4130 steel with an alternate ferrite/pearlite banded structure, Mater. Sci. Eng. A 142 (2) (1991) 193–201.
[20] L. Tau, S. Chan, Effects of ferrite/pearlite alignment on the hydrogen permeation in a AISI 4130 steel, Mater. Lett. 29 (1-3) (1996) 143–147.
[21] J. Toribio, D. Vergara, M. Lorenzo, Influence of loading rate on the hydrogen-assisted micro-damage in bluntly notched samples of pearlitic steel, Metals 6 (1) (2016) 11.
[22] R.A. Oriani, The diffusion and trapping of hydrogen in steel, Acta Metall. 18 (1) (1970) 147–157.
[23] N. Winzer, O. Rott, R. Thiessen, I. Thomas, K. Mraczek, T. Hoche, L. Wright, M. Mrovec, Hydrogen diffusion and trapping in Ti-modified advanced high strength steels, Mater. Des. 92 (2016) 450–461.
[24] A. Turk, D. Bombac, J.J. Rydel, M. Zietara, P.E. Rivera-Diaz-del Castillo, E.I. Galindo-Nava, Grain boundary carbides as hydrogen diffusion barrier in a Fe-Ni alloy: a thermal desorption and modelling study, Mater. Des. 160 (2018) 985–998.
[25] J. Toribio, V. Kharin, A generalised model of hydrogen diffusion in metals with multiple trap types, Philos. Mag. 95 (31) (2015) 3429–3451.
[26] G. Pressouyre, Trap theory of hydrogen embrittlement, Acta Metall. 28 (7) (1980) 895–911.
[27] J. Takahashi, K. Kawakami, Y. Kobayashi, T. Tarui, The first direct observation of hydrogen trapping sites in TiC precipitation-hardening steel through atom probe tomography, Scr. Mater. 63 (3) (2010) 261–264.
[28] B. Szost, R. Vegter, P. Rivera-Diaz-del Castillo, Developing bearing steels combining hydrogen resistance and improved hardness, Mater. Des. 43 (2013) 499–506.
[29] X. Shi, W. Yan, W. Wang, Y. Shan, K. Yang, Novel Cu-bearing high-strength pipeline steels with excellent resistance to hydrogen-induced cracking, Mater. Des. 92 (2016) 300–305.
[30] W. Choo, J.Y. Lee, Thermal analysis of trapped hydrogen in pure iron, Metall. Trans. A. 13 (1) (1982) 135–140.
[31] D. Johnson, J. Wu, Hydrogen transport in carbon steels as a function of carbon content and heat treatment near 298 K, J. Mater. Energy Syst. 8 (4) (1987) 402–408.
[32] J. Wu, Electrochemical method for studying hydrogen in iron, nickel and palladium, Int. J. Hydrog. Energy 17 (12) (1992) 917–921.
[33] K.-i. Ebihara, T. Suzudo, H. Kaburaki, K. Takai, S. Takebayashi, Modeling of hydrogen thermal desorption profile of pure iron and eutectoid steel, ISIJ Int. 47 (8) (2007) 1131–1140.
[34] S. Frappart, X. Feaugas, J. Creus, F. Thebault, L. Delattre, H. Marchebois, Hydrogen solubility, diffusivity and trapping in a tempered Fe-C-Cr martensitic steel under various mechanical stress states, Mater. Sci. Eng. A 534 (2012) 384–393.
[35] W. Choo, Effect of cathodic charging current density on the apparent hydrogen diffusivity through pure iron, J. Mater. Sci. 19 (8) (1984) 2633–2638.
[36] S.-M. Lee, J.-Y. Lee, The trapping and transport phenomena of hydrogen in nickel, Metall. Trans. A. 17 (2) (1986) 181–187.
[37] H.E. Kissinger, Reaction kinetics in differential thermal analysis, Anal. Chem. 29 (11) (1957) 1702–1706.
[38] A. McNabb, P. Foster, A new analysis of the diffusion of hydrogen in iron and ferritic steels, Trans. Metall. Soc. AIME 227 (3) (1963) 618–627.
[39] J. Leblond, D. Dubois, A general mathematical description of hydrogen diffusion in steels-I. Derivation of diffusion equations from Boltzmann-type transport equations, Perspectives in Hydrogen in Metals, Elsevier. 1986, pp. 193–203.
[40] J. Leblond, D. Dubois, A general mathematical description of hydrogen diffusion in steels-II. Numerical study of permeation and determination of trapping parameters, Perspectives in Hydrogen in Metals, Elsevier. 1986, pp. 205–212.
[41] M. Dadfarnia, P. Sofronis, T. Neeraj, Hydrogen interaction with multiple traps: can it be used to mitigate embrittlement? Int. J. Hydrog. Energy 36 (16) (2011) 10141–10148.
[42] F. Fischer, J. Svoboda, E. Kozeschnik, Interstitial diffusion in systems with multiple sorts of traps, Model. Simul. Mater. Sci. Eng. 21 (2) (2013) 025008.
[43] E.J. Song, D.-W. Suh, H. Bhadeshia, Theory for hydrogen desorption in ferritic steel, Comput. Mater. Sci. 79 (2013) 36–44.
[44] A. Kumnick, H. Johnson, Deep trapping states for hydrogen in deformed iron, Acta Metall. 28 (1) (1980) 33–39.
[45] A. Turnbull, R. Hutchings, D. Ferriss, Modelling of thermal desorption of hydrogen from metals, Mater. Sci. Eng. A 238 (2) (1997) 317–328.
[46] T. Depover, O. Monbaliu, E. Wallaert, K. Verbeken, Effect of Ti, Mo and Cr based precipitates on the hydrogen trapping and embrittlement of Fe-C-X Q&T alloys, Int. J. Hydrog. Energy 40 (47) (2015) 16977–16984.
[47] E. Galindo-Nava, B. Basha, P. Rivera-Díaz-del Castillo, Hydrogen transport in metals: integration of permeation, thermal desorption and degassing, J. Mater. Sci. Technol. 33 (12) (2017) 1433–1447.
[48] S. Frappart, X. Feaugas, J. Creus, F. Thebault, L. Delattre, H. Marchebois, Study of the hydrogen diffusion and segregation into Fe-C-Mo martensitic HSLA steel using electrochemical permeation test, J. Phys. Chem. Solids 71 (10) (2010) 1467–1479.
[49] D.A. Porter, K.E. Easterling, M. Sherif, Phase Transformations in Metals and Alloys, (Revised Reprint), CRC press. 2009.
[50] E. Legrand, J. Bouhattate, X. Feaugas, H. Garmestani, Computational analysis of geometrical factors affecting experimental data extracted from hydrogen permeation tests: II-consequences of trapping and an oxide layer, Int. J. Hydrog. Energy 37 (18) (2012) 13574–13582.
[51] H. Hagi, Y. Hayashi, N. Ohtani, Diffusion coefficient of hydrogen in pure iron between 230 and 300 K, Trans. Jpn. Inst. Metals 20 (7) (1979) 349–357.
[52] S.M. Charca, O.N. Uwakweh, V.S. Agarwala, Hydrogen transport conditions and effects in cathodically polarized AF1410 steel, Metall. Mater. Trans. A 38 (10) (2007) 2389–2399.
[53] Y. Furuya, E. Hashimoto, T. Kino, Hydrogen permeation through Nickel, Jpn. J. Appl. Phys. 23 (9R) (1984) 1190.
[54] J. Xu, X. Sun, W. Chen, Y. Li, Hydrogen permeation and diffusion in iron-base superalloys, Acta Metall. Mater. 41 (5) (1993) 1455–1459.
[55] S. Wang, N. Hashimoto, Y. Wang, S. Ohnuki, Activation volume and density of mobile dislocations in hydrogen-charged iron, Acta Mater. 61 (13) (2013) 4734–4742.
[56] J. Tien, A.W. Thompson, I. Bernstein, R.J. Richards, Hydrogen transport by dislocations, Metall. Trans. A. 7 (6) (1976) 821–829.
[57] N. Parvathavarthini, S. Saroja, R. Dayal, H. Khatak, Studies on hydrogen permeability of 2.25% Cr-1% Mo ferritic steel: correlation with microstructure, J. Nucl. Mater. 288 (2-3) (2001) 187–196.
[58] M.A. Stopher, P. Lang, E. Kozeschnik, P.E. Rivera-Diaz-del Castillo, Modelling hydrogen migration and trapping in steels, Mater. Des. 106 (2016) 205–215.
[59] G.-W. Hong, J.-Y. Lee, The interaction of hydrogen and the cementite-ferrite interface in carbon steel, J. Mater. Sci. 18 (1) (1983) 271–277.
[60] B. Szost, R. Vegter, P.E. Rivera-Díaz-del Castillo, Hydrogen-trapping mechanisms in nanostructured steels, Metall. Mater. Eng. 44 (10) (2013) 4542–4550.